

A multi-band and polarization-independent perfect absorber based on Dirac semimetals circles and semi-ellipses array

Zhiyou Li(李治友), Yingting Yi(易颖婷), Danyang Xu(徐丹阳), Hua Yang(杨华), Zao Yi(易早), Xifang Chen(陈喜芳), Yougen Yi(易有根), Jianguo Zhang(张建国), and Pinghui Wu(吴平辉)

Citation: Chin. Phys. B, 2021, 30 (**9**): 098102. DOI: 10.1088/1674-1056/abfb57
Journal homepage: http://cpb.iphy.ac.cn; http://iopscience.iop.org/cpb

What follows is a list of articles you may be interested in

Dynamically tunable terahertz passband filter based on metamaterials integrated with a graphene middle layer

MaoSheng Yang(杨茂生), LanJu Liang(梁兰菊), DeQuan Wei(韦德泉), Zhang Zhang(张璋), Xin Yan(闫昕), Meng Wang(王猛), JianQuan Yao(姚建铨)
Chin. Phys. B, 2018, 27 (**9**): 098101. DOI: 10.1088/1674-1056/27/9/098101

Robust stability characterizations of active metamaterials with non-Foster loads

Yi-Feng Fan(范逸风), Yong-Zhi Sun(孙永志)
Chin. Phys. B, 2018, 27 (**2**): 028102. DOI: 10.1088/1674-1056/27/2/028102

Polarization-insensitive unidirectional spoof surface plasmon polaritons coupling by gradient metasurface

Hong-yu Shi(施宏宇), An-xue Zhang(张安学), Jian-zhong Chen(陈建忠), Jia-fu Wang(王甲富), Song Xia(夏颂), Zhuo Xu(徐卓)
Chin. Phys. B, 2016, 25 (**7**): 078105. DOI: 10.1088/1674-1056/25/7/078105

Tri-band transparent cross-polarization converters using a chiral metasurface

Shi Hong-Yu, Li Jian-Xing, Zhang An-Xue, Wang Jia-Fu, Xu Zhuo
Chin. Phys. B, 2014, 23 (**11**): 118101. DOI: 10.1088/1674-1056/23/11/118101

Tunable ultra-wideband terahertz filter based on three-dimensional arrays of H-shaped plasmonic crystals

Yuan Cai, Xu Shi-Lin, Yao Jian-Quan, Zhao Xiao-Lei, Cao Xiao-Long, Wu Liang
Chin. Phys. B, 2014, 23 (**1**): 018102. DOI: 10.1088/1674-1056/23/1/018102

A multi-band and polarization-independent perfect absorber based on Dirac semimetals circles and semi-ellipses array*

Zhiyou Li(李治友)[1,†], Yingting Yi(易颖婷)[3,†], Danyang Xu(徐丹阳)[4], Hua Yang(杨华)[2], Zao Yi(易早)[1,‡], Xifang Chen(陈喜芳)[1], Yougen Yi(易有根)[3], Jianguo Zhang(张建国)[5], and Pinghui Wu(吴平辉)[6,§]

[1] *Joint Laboratory for Extreme Conditions Matter Properties, Southwest University of Science and Technology, Mianyang* 621010, *China*
[2] *State Key Laboratory of Advanced Processing and Recycling of Non-ferrous Metals, Lanzhou University of Technology, Lanzhou* 730050, *China*
[3] *College of Physics and Electronics, Central South University, Changsha* 410083, *China*
[4] *College of Science, Zhejiang University of Technology, Hangzhou* 310023, *China*
[5] *Department of Physics and Electronic Engineering, Jinzhong University, Jinzhong* 030619, *China*
[6] *Research Center for Photonic Technology, Key Laboratory of Information Functional Material for Fujian Higher Education, Quanzhou Normal University, Quanzhou* 362000, *China*

(Received 23 February 2021; revised manuscript received 5 April 2021; accepted manuscript online 26 April 2021)

We design a four-band terahertz metamaterial absorber that relied on the block Dirac semi-metal (BDS). It is composed of a Dirac material layer, a gold reflecting layer, and a photonic crystal slab (PCS) medium layer. This structure achieved perfect absorption of over 97% at 4.06 THz, 6.15 THz, and 8.16 THz. The high absorption can be explained by the localized surface plasmon resonance (LSPR). And this conclusion can be proved by the detailed design of the surface structure. Moreover, the resonant frequency of the device can be dynamically tuned by changing the Fermi energy of the BDS. Due to the advantages such as high absorption, adjustable resonance, and anti-interference of incident angle and polarization mode, the Dirac semi-metal perfect absorber (DSPA) has great potential value in fields such as biochemical sensing, information communication, and nondestructive detection.

Keywords: metamaterials, terahertz, block Dirac semi-metal, localized surface plasmon resonance

PACS: 81.05.Xj, 87.50.up, 36.20.Kd, 73.20.Mf **DOI:** 10.1088/1674-1056/abfb57

1. Introduction

Metamaterials have properties of negative permittivity and negative permeability.[1] At present, the properties of electromagnetic stealth and negative refractive index of metamaterials have been successfully verified.[2–4] Since Landy *et al.* first reported metamaterials based on perfect absorbers in 2008,[5] there are many applications for metamaterial absorbers in different spectral ranges, such as sensors, infrared detectors, and other devices.[6,7] Researches on metamaterial absorbents based on the plasmon element theory have been quite extensive.[8,9] In 2010, Hao *et al.* reported an ultra-thin, wide-angle metamaterial optical frequency absorber.[10] Yao *et al.* proposed an absorber with a periodic pattern-elliptic disk graphene structure.[11] However, it requires high processing technology, which limits its wide application. At present, to avoid the disadvantage of the three-dimensional (3D) structure of metamaterials in the loss, scientists put forward the concept of metasurfaces,[12–15] and achieved some successful research results in high-efficiency metasurfaces,[16–18] but three-dimensional block metamaterials still have its unique advantages.

The 3D Dirac semi-metals[19] can be viewed as a 3D graphene analog, its status can be converted between dielectric response and metallic properties by adjusting E_F.[20] When the electron frequency in BDS is consistent with the frequency of incident light, the surface plasmon polaritons (SPPs)[21] will be excited. By changing E_F through adjusting the extra bias voltage, the BDS of permittivity functions can be adjusted.[22–24]

In this paper, a DSPA is designed, which is composed of BDS array superposition on the metal layer and insulator support material. The results obtained from CST Microwave Studio show that there are three perfect absorption peaks above 97%. These three absorption peaks can be reasonably explained by the LSPR coupling of the BDS structure. Our absorber has more advantages in practical application due to its simpler structure and better polarization angle adaptability.

*Project supported by the National Natural Science Foundation of China (Grant Nos. 11604311, 61705204, and 21506257), the Scientific Research Fund from Sichuan Provincial Science and Technology Department (Grant Nos. 2020YJ0137 and 2020YFG0467), the Undergraduate Innovation Fund by Southwest University of Science and Technology (Grant No. JZ20-027), the Fund by the School of Science of Southwest University of Science and Technology for the Innovation Fund Project (Grant No. LX2020010), and the Undergraduate Innovation and Entrepreneurship Training Program of Southwest University of Science and Technology (Grant No. S202010619073).

†These authors contributed equally to this work.
‡Corresponding author. E-mail: yizaomy@swust.edu.cn
§Corresponding author. E-mail: wph1021@163.com

© 2021 Chinese Physical Society and IOP Publishing Ltd

2. Structure and design

The absorber consists of the BDS layer, PCS layer, and gold (Au) layer, in which the BDS layer is composed of four semi-elliptic columns and a central cylinder (3D model and top view are shown in Figs. 1(a) and 1(b). We used the finite element method (FEM) solver based on CST Microwave Studio to analyze the simulation results and used a Fermi level $E_F = 65$ meV for BDS. The refractive index of PCS is $n = 3.416$. The absorber adopts the polarization form of the incident plane wave k along the direction of the $-z$ axis and the electric field E along the direction of the x axis. The parameters in sequence as follows: $a = 3.24$ μm, $b = 1.08$ μm, $D = 3.6$ μm, $h_1 = 0.375$ μm, $h_2 = 2.25$ μm, $h_3 = 0.1$ μm, and the periods $P_x = P_y = 9$ μm.

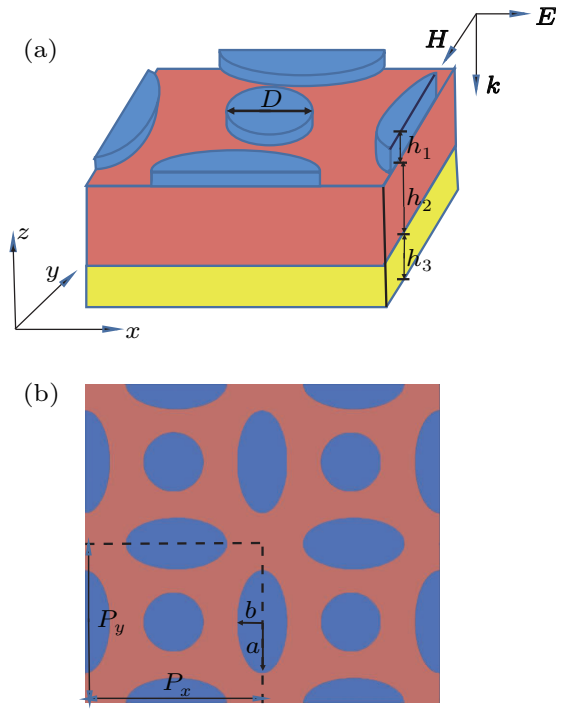


Fig. 1. (a) The multi-peak DSPA 3D diagram and (b) the plan of DSPA in the x–y plane.

According to the Kubo model in stochastic phase approximation theory, when horizontal operations are not considered and in the low-temperature limit $T \ll E_F$, the approximate expression of local dynamic conductivity σ of BDS can be obtained as

$$\mathrm{Re}\left(\sigma\left(\Omega\right)\right) = \frac{e^2}{\hbar}\frac{gk_F}{24\pi}\Omega\theta\left(\Omega - 2\right), \tag{1}$$

$$\mathrm{Im}\left(\sigma\left(\Omega\right)\right) = \frac{e^2}{\hbar}\frac{gk_F}{24\pi^2}\left[\frac{4}{\Omega} - \Omega\ln\left(\frac{4E_c^2}{|\Omega^2 - 4|}\right)\right], \tag{2}$$

where $k_F = E_F/\hbar v_F$ is the Fermi momentum, $v_F \approx c/300$ is the Fermi velocity. Considering the Drude damping

$$\Omega = \hbar\omega/E_F + \mathrm{i}\hbar\tau^{-1}/E_F,$$

the carrier mobility μ can control scattering rate

$$\hbar\tau^{-1} = v_F/(k_F\mu), \quad \varepsilon_c = E_c/E_F,$$

where E_c stands for the cut-off energy when the Dirac spectrum starts to become nonlinear, $g = 40$ is the degeneracy factor.[25] Applying the two-band model, we obtain the permittivity of BDS[26]

$$\varepsilon = \varepsilon_b + \mathrm{i}\sigma/\omega\varepsilon_0, \tag{3}$$

where $\varepsilon_b = 1$.

3. Results and discussion

There is almost no transmission in the absorber ($T = 0$) because gold is thick enough. We only need to calculate the reflectivity (R), and then define the absorptivity A[27] by using $1 - R$.

The optical response comparison of two polarization modes (TE and TM polarizations) at 65-meV energy is obtained in Fig. 2(a). The resonance frequencies are $f_{R1} = 4.06$ THz, $f_{R2} = 6.15$ THz, $f_{R3} = 8.16$ THz, and $f_{R4} = 9.76$ THz, corresponding to multimode absorption with absorption rates of 98%, 97.7%, 99.99%, and 71%. The absorption spectra are highly coincident under the two polarizations, which are determined by the rotational symmetry of the absorber. Also, we have studied the relationship between LSPR and incident angles in different polarization modes (TE and TM modes) by constantly scanning from 0° to 80° in Figs. 2(b) and 2(c). We can see that the absorber has good incident angle tolerance characteristics. Besides, there is a good robustness characteristic in Fig. 2(b). As for TE polarization, the absorption spectrum begins to fade and become sharp at a higher incidence angle. Based on the LSPR theory, the magnetic field tangential component decreases as the incidence angle θ increases, which ultimately leads to the weakening and disappearance of resonance. A similar process also occurs in TM mode. The increased frequency range of the absorption band in TM mode and the occurrence of a partial blue shift can be considered as the occurrence of a partial parasitic resonance.

Based on the LSPR, the absorption enhancement can be studied by the surface electric field distribution at the resonance frequency. We calculated the electric field distribution at three resonant frequencies with an absorption intensity greater than 97%.

Figures 3(a)–3(c) show the surface electric field intensity distribution at the resonant frequencies of 4.06 THz, 6.15 THz, and 8.16 THz. The electric field is concentrated at the long axis boundary of the semi-ellipse in the x direction at resonance f_{R1}. At resonant mode f_{R2}, the electric field is bound in the y direction of the central Dirac disk. At mode f_{R3}, the electric field constraint region is at the boundary of the short axis of the BDS semi-ellipse in the y direction. With the increase of frequency, the coupling region of the electric field at

the interface between BDS and the medium is different, which indicates that the excitation of multiple modes is caused by the difference of surface BDS structural regions, and they are independent of each other. From the maximum value of the local electric field, the regional electric field will also increase under the higher resonance mode. We can conclude that the coupling effect between Dirac semi-metal and the electric field is stronger at high frequencies due to LSPR.

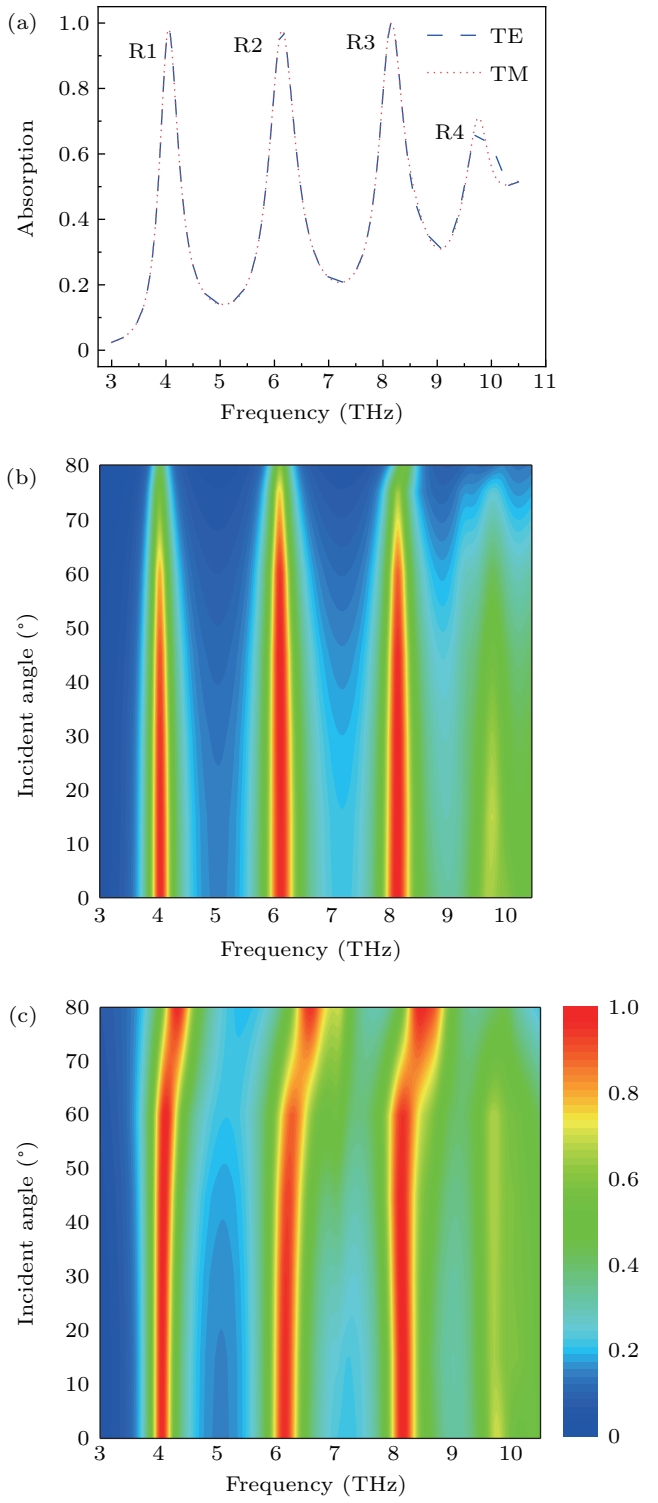


Fig. 2. (a) TE and TM absorption spectra, (b) the relationship between LSPR and incident angle in TE mode, (c) the relationship between LSPR and incident angle in TM mode.

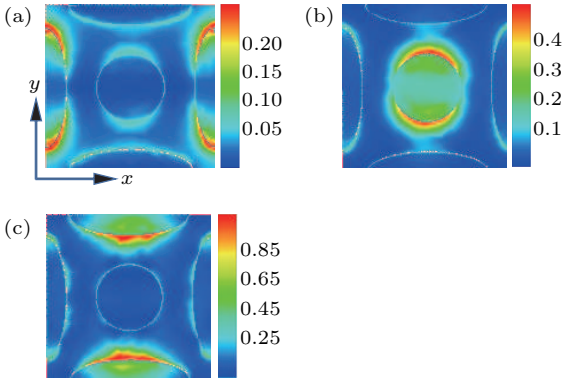


Fig. 3. The electric field distribution in the x–y plane at three resonant frequencies: (a) 4.06 THz, (b) 6.15 THz, (c) 8.16 THz with an absorption intensity greater than 97%. The dotted line is the boundary between BDS and PCS.

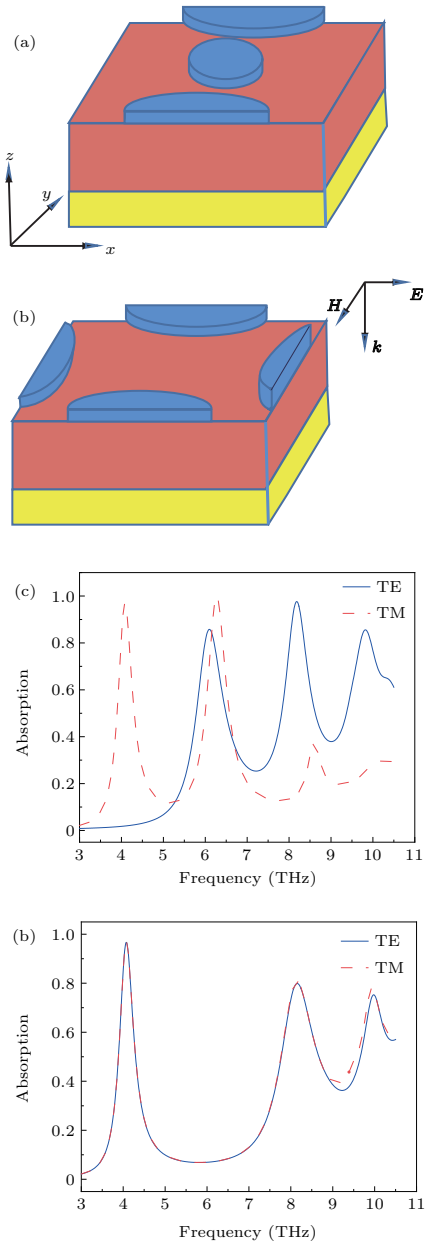


Fig. 4. (a) The structure drawing after eliminating the BDS semi-ellipse in the x direction, (b) the structure drawing after eliminating the BDS central cylinder. (c) the DASP absorption spectrum of lacking BDS semi-ellipse in the x direction, (d) the DASP absorption spectrum of lacking BDS central cylinder.

To better analyze the coupling between the absorber and the plane wave, we conducted a more detailed study on the specific effect of the Dirac array structure on the surface of the absorber on the electromagnetic energy absorption. Therefore, the arrays composed of Dirac circle and semi-ellipse were selectively retained and their absorption spectra were explored.

In Figs. 4(a) and 4(b), the structural schematic plots of BDS semi-ellipse and central cylinder eliminating in the TE polarization direction are shown respectively. In Fig. 4(c) we obtained the wave absorption of the absorber without the x-direction BDS ellipse through the software CST simulation numerical simulation. We define it as case 1. When a pair of symmetric semi-elliptical BDS structures in the x direction is not introduced, the absorption spectrum of this absorber is much different from the original spectrum shown in Fig. 2(a). In TE mode, the electric resonance no longer occurs at 4.06 THz, and the original modes R2 and R3 still exist. On the contrary, in TM mode, the electric resonance near 8.16 THz almost disappears, while the original modes R1 and R2 still appear. This inconsistency can be attributed to the destruction of the original rotational symmetry with the disappearance of the x-direction semi-elliptical symmetry array.

Figure 4(d) is the normal incident spectrum of the other case in which only the semi-elliptical cylindrical BDS structure around is retained while the central cylinder is not placed, which is defined as case 2. It is observed that the original R2 has disappeared in both TE and TM polarizations, and the two main resonance modes, R1 and R3, still exist. This phenomenon can be judged as the disappearance of R2 resonance due to the absence of central cylinder support.

In Figs. 5(a) and 5(b), it can be seen that the absorption of LSPR does not occur because the electric field $\boldsymbol{E}$ direction of TE is consistent with the direction x and there is no support of semi-elliptical structure in the direction x at R1 = 4.06 THz. In TM polarization, the direction of the electric field is consistent with the positive y direction, so the structure provides suitable LSPR conditions. Figures 5(c) and 5(d) show that the perfect absorber at 8.16 THz is influenced by the $-y$ magnetic resonance. In the case of TE polarization, the magnetic field still produces a resonance effect in the $-y$ direction of the BDS layer. Since the y-direction BDS semi-ellipse structure always exists, the strong absorption of plane waves can be generated. As the magnetic field $\boldsymbol{H}$ is in the x direction, there is no LSPR resonance structure corresponding to it in the x direction, so strong plasmon resonance will not occur under TM polarization. In conclusion, the results in Figs. 5(a)–5(d) are completely consistent with those in Fig. 4(c).

On the other hand, in Figs. 5(e)–5(f), the structure of rotational symmetry is very obvious. In the absence of a central BDS surface cylinder, the absorber's absorbing capacity at 6.15 THz was significantly reduced. This result proved that the R2 resonance in Figs. 2(a) and 3(b) is mainly caused by the central Dirac cylinder structure.

We know that the conductivity is a function of the Fermi energy from Eqs. (1) and (2). Therefore, the dynamic conductivity distribution of BDS can be affected by adjusting the Fermi energy of BDS, and then its dielectric constant can be changed. Finally, the resonance absorption state based on *LSPR* can be adjusted.

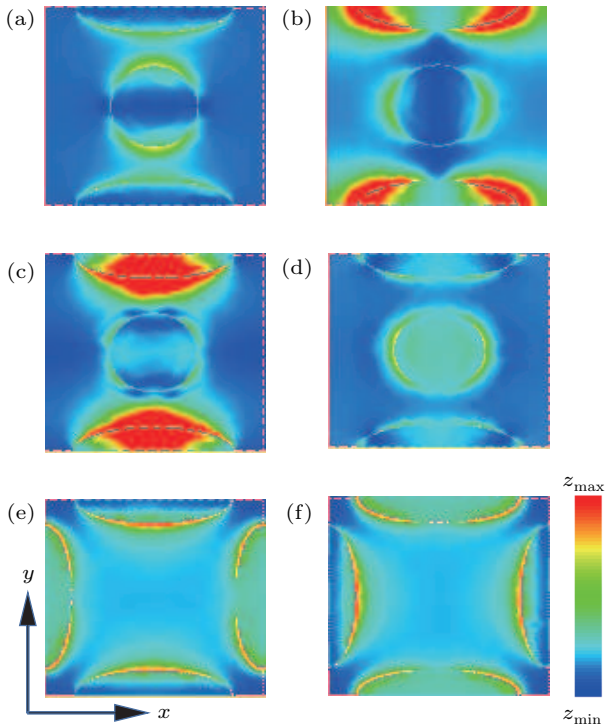


Fig. 5. (a)–(b) Surface electric field distribution at 4.06 THz under TE and Tm polarizations in case 1, (c)–(d) surface electric field distribution at 8.16 THz under TM and Tm polarizations in case 1, (e)–(f) surface electric field distribution at 6.15 THz in case 2.

The spectral response at five different E_{F}, 50 meV, *i.e.*, 55 meV, 60 meV, 65 meV, and 70 meV, is shown in Fig. 6(a). In Fig. 6(b), it can be seen that the trends are similar for the three modes. The absorption intensity increases first and then decreases under the condition of increasing Fermi level. The reason is that the impedance relationship between the absorber and the free space presents a process of first approaching and then alienating with the increase of Fermi energy.[28] The R2 mode still maintains a high absorption of more than 91.7%, while the resonance absorption of R1 and R3 modes is greatly improved in the range of 50 meV to 70 meV. With E_{F} increasing, absorption modes have different degrees of blue shift. As shown in Fig. 6(c), the blue shift of the three modes is similar as the Fermi energy increases from 50 meV to 70 meV, and the average offset is 1.476 THz. The reason of blue sheft can be explained by LC model.[29] As the Fermi level increases, the effective index n_{sp} for BDS decreases, which ultimately leads to an increase in the resonance frequency. The above calculations fully illustrate the tunable characteristics of the device we designed.

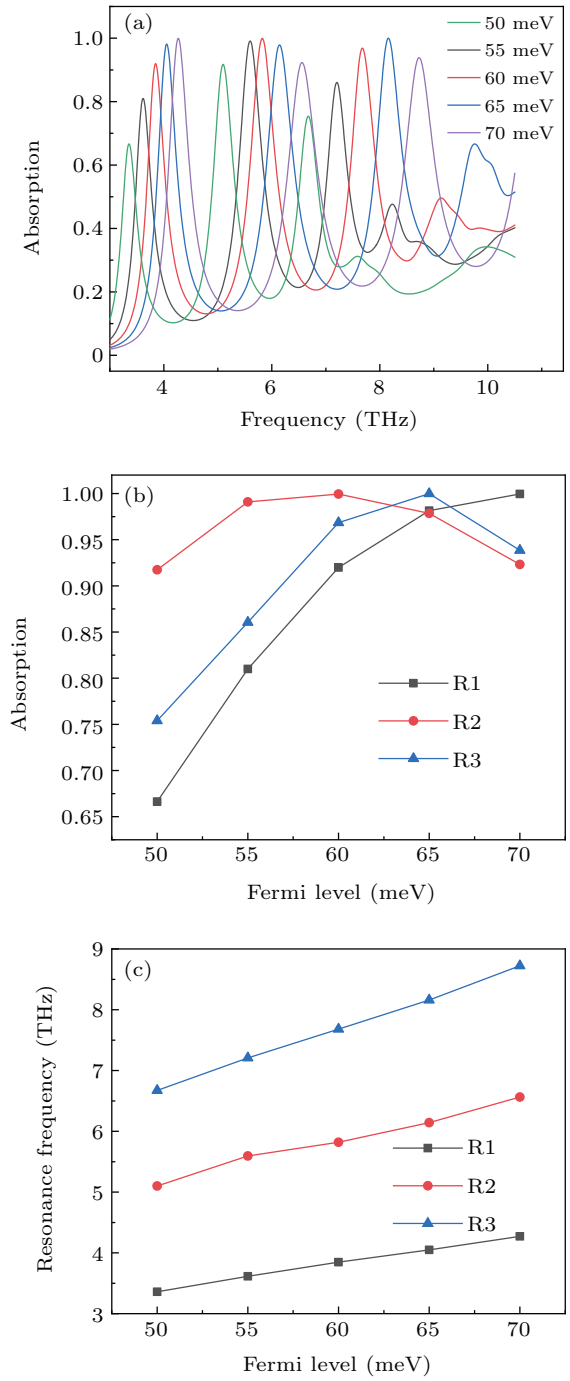


Fig. 6. (a) Absorption spectra corresponding to the absorber at different BDS Fermi levels, (b) the absorption intensity varies with the Fermi level, (c) the shift of the three resonant frequencies with the increase of Fermi level.

4. Conclusion

We have explored a special perfect absorber relied on the Dirac array. Our results show that at $E_F = 65$ meV, three perfect absorption modes of over 97% can be achieved. The multi-peak absorption can be attributed to the LSPR excited. The resonance mode of the absorber is the result of the interaction between the cylinder and the semi-elliptical cylinder composed of BDS. As E_F increases, the spectral response of the absorber has different degrees of blue shift. Due to its advanced features such as adjustable absorption peak, simple structure, and incident angle tolerability, it possesses good prospects in biochemical sensing, THz wave communication, and environmental monitoring.

References

[1] Qi Y P, Zhang B H, Ding J H, Zhang T, Wang X X and Yi Z 2021 *Chin. Phys. B* **30** 024211
[2] Zhang Y B, Yi Z, Wang X Y, Chu P X, Yao W T, Zhou Z G, Cheng S B, Liu Z M, Wu P H, Pan M and Yi YG 2021 *Physica E* **127** 114526
[3] Jiang L Y, Yuan C, Li Z Y, Su J, Yi Z, Yao W T, Wu P H, Liu Z M, Cheng S B and Pan M 2021 *Diam. Relat. Mater.* **111** 108227
[4] Wang X X, Zhu J K, Xu Y Q, Qi Y P, Zhang L P, Yang H and Yi Z 2021 *Chin. Phys. B* **30** 024207
[5] Landy N I, Sajuyigbe S, Mock J J, Smith D R and Padilla W J 2008 *Phys. Rev. Lett.* **100** 207402
[6] Yi Z, Li J K, Lin J C, Qin F, Chen X F, Yao W T, Liu Z M, Cheng S B, Wu P H and Li H L 2020 *Nanoscale* **12** 23077
[7] Li J K, Chen X F, Yi Z, Yang H, Tang Y J, Yi Y, Yao W T, Wang J Q and Yi Y G 2020 *Mater. Today Energy* **16** 100390
[8] Yu P Q, Yang H, Chen X F, Yi Z, Yao W T, Chen J F, Yi Y G and Wu P H 2020 *Renew. Energy* **158** 227
[9] Zhao F, Chen X F, Yi Z, Qin F, Tang Y J, Yao W T, Zhou Z G and Yi Y G 2020 *Solar Energy* **204** 635
[10] Hao J M, Wang J, Liu X L, Padilla W J, Zhou L and Qiu M 2010 *Appl. Phys. Lett.* **96** 251104
[11] Yao, G, Ling F R, Yue J, Luo C Y, Ji J and Yao J Q 2016 *Opt. Express* **24** 1518
[12] Kildishev A V, Boltasseva A and Shalaev V M 2013 *Science* **339** 1232009
[13] Zhang Y B, Wu P H, Zhou Z G, Chen X F, Yi Z, Zhu J Y, Zhang T S and Jile H 2020 *IEEE Access* **8** 85154
[14] Qin F, Chen X F, Yi Z, Yao W T, Yang H, Tang Y J, Yi Y, Li H L and Yi YG 2020 *Sol. Energy Mater. Sol. Cells* **211** 110535
[15] Cen C L, Zhang Y B, Chen X F, Yang H, Yi Z, Yao W T, Tang Y J, Yi Y G, Wang J Q and Wu P H 2020 *Physica E* **117** 113840
[16] Lin B Q, Guo J X, Huang B G, Fang L B, Chu P and Liu X W 2018 *Chin. Phys. B* **27** 054204
[17] Khan M I and Tahir F A 2018 *Chin. Phys. B* **27** 014101
[18] Hou H S, Wang G M, Li H P, Guo W L, Li T J and Cai T 2017 *Chin. Phys. B* **26** 057701
[19] Young S M, Zaheer S, Teo J C Y, Kane C L, Mele E J and Rappe A M 2012 *Phys. Rev. Lett.* **108** 140405
[20] Wang Y Q, Yi Y T, Xu D Y, Yi Z, Li Z Y, Chen X F, Jile H, Zhang J G, Zeng L C and Li G F 2021 *Physica E* **131** 114750
[21] Zhang J X, Zhang L D and Xu W 2012 *J. Phys. D: Appl. Phys.* **45** 113001
[22] Wu Y F, Zhang L, Li C Z, Zhang Z S, Liu S, Liao Z M and Yu D P 2018 *Adv. Mater.* **30** 1707547
[23] Chen Z H, Chen H, Jile H, Xu D Y, Yi Z, Lei Y L, Chen X F, Zhou Z G, Cai S S and Li G F 2021 *Diam. Relat. Mater.* **115** 108374
[24] Chen H, Zhang H, Liu M, Zhao Y, Guo X and Zhang Y 2017 *Opt. Mater. Express* **7** 3397
[25] Timusk T, Carbotte J P, Homes C C, Basov D N and Sharapov S G 2013 *Phys. Rev. B* **87** 235121
[26] Chen H, Zhang H Y, Liu M D, Zhao Y K, Guo X H and Zhang Y P 2017 *Opt. Mater. Express* **7** 3397
[27] Chu P X, Chen J X, Xiong Z G and Yi Z 2020 *Opt. Commun.* **476** 126338
[28] Vasi B and Gaji R 2013 *Appl. Phys. Lett.* **103** 261111
[29] Hossain M.B, Mehedi I M, Moznuzzaman M, Abdulrazak L F and Hossain M D 2019 *Results Phys.* **15** 102719